

Title	Solid state pathways to complex shape evolution and tunable porosity during metallic crystal growth
Authors	Valenzuela, Carlos Díaz;Carriedo, Gabino A.;Valenzuela, María Luisa;Zúñiga, Luis;O'Dwyer, Colm
Publication date	2013-09-12
Original Citation	Valenzuela, C. D., Carriedo, G. A., Valenzuela, M. L., Zúñiga, L. and O'Dwyer, C. (2013) 'Solid State Pathways to Complex Shape Evolution and Tunable Porosity during Metallic Crystal Growth', Scientific Reports, 3, 2642 (8pp). doi: 10.1038/srep02642
Type of publication	Article (peer-reviewed)
Link to publisher's version	10.1038/srep02642
Rights	© 2013 The Authors. This work is licensed under a Creative Commons Attribution-NonCommercial-ShareALike 3.0 Unported License. To view a copy of this license, visit http://creativecommons.org/licenses/by-nc-sa/3.0/ - http://creativecommons.org/licenses/by-nc-sa/3.0/
Download date	2023-05-07 20:32:07
Item downloaded from	https://www.nature.com/articles/srep02642



UCC

University College Cork, Ireland
 Coláiste na hOllscoile Corcaigh



OPEN

SUBJECT AREAS:
NANOSCALE MATERIALS
MATERIALS SCIENCE
MATERIALS CHEMISTRY

Solid State Pathways to Complex Shape Evolution and Tunable Porosity during Metallic Crystal Growth

Carlos Díaz Valenzuela¹, Gabino A. Carriedo², María L. Valenzuela³, Luis Zúñiga⁴ & Colm O'Dwyer^{5,6,7}

Received
2 August 2013

Accepted
27 August 2013

Published
12 September 2013

Correspondence and
requests for materials
should be addressed to
C.O.D. (c.odwyer@
ucc.ie) or C.D.V.
(cdiaz@uchile.cl)

¹Departamento de Química, Facultad de Ciencias, Universidad de Chile, Casilla 653, Santiago, Chile, ²Departamento de Química Orgánica e Inorgánica, Facultad de Química, Universidad de Oviedo, C/Julián Clavería S/N, Oviedo 3307, Spain, ³Universidad Andres Bello, Departamento de Ciencias Químicas, Facultad de Ciencias, Av. Republica 275, Santiago, Chile, ⁴Departamento de Física, Universidad de Chile, Facultad de Ciencias Físicas y Matemáticas, Blanco Encalada 2008, Santiago, Chile, ⁵Department of Chemistry, University College Cork, Cork, Ireland, ⁶Materials and Surface Science Institute, University of Limerick, Limerick, Ireland, ⁷Micro and Nanoelectronics Centre, Tyndall National Institute, Lee Maltings, Cork, Ireland.

Growing complex metallic crystals, supported high index facet nanocrystal composites and tunable porosity metals, and exploiting factors that influence shape and morphology is crucial in many exciting developments in chemistry, catalysis, biotechnology and nanoscience. Assembly, organization and ordered crystallization of nanostructures into complex shapes requires understanding of the building blocks and their association, and this relationship can define the many physical properties of crystals and their assemblies. Understanding crystal evolution pathways is required for controlled deposition onto surfaces. Here, complex metallic crystals on the nano- and microscale, carbon supported nanoparticles, and spinodal porous noble metals with defined inter-feature distances in 3D, are accomplished in the solid-state for Au, Ag, Pd, and Re. Bottom-up growth and positioning is possible through competitive coarsening of mobile nanoparticles and their site-specific crystallization in a nucleation-dewetted matrix. Shape evolution, density and growth mechanism of complex metallic crystals and porous metals can be imaged during growth.

Metallic nanocrystals with complex polyhedral shapes^{1–3} have seen a surge in development^{3–5}, owing to the lure of exotic and genuinely useful properties ranging from chemistry³ to optics, and catalysis^{6,7} to biomedical labeling, and high throughput combinatorial biotechnological^{8,9} and other useful applications where the nanoscale feature morphology and topology greatly influences performance¹⁰. The exquisite control now possible using solution-based methods^{11,12} allows a myriad of complex shapes¹³ using well-developed design rules^{14,15} to control selective deposition onto specific crystallographic faces of the crystal using surfactants or ligands^{11,14}. Crystals with complex shapes and composition have been made possible through the development of highly controllable protocols and design rules for their synthesis⁵ in solutions. Standard methods require controlled seeding² and growth tuned by surfactants, with a strong dependence on the seed, which is sometimes a different material⁴. The dependence on solution-based methods limits the possibility of achieving similar and indeed new structures, some thermodynamically impossible in solution, in the solid state and on larger length scales. Solution-free, ‘dry’ syntheses are a necessity for some investigations and applications. Solution approaches offer bespoke shape design by relying on chemical engineering of homo- and heterogeneous phases or seeds, which must be single crystal¹⁶. Complex Platonic shapes¹⁷ are often best controlled if the nucleation seeds themselves consist of significant complexity in shape and growth pathways were very recently observed when nanocrystal growth in solutions was monitored in real-time⁴. Understanding how nanoscale particles can associate during a complex decomposition process of a solid state precursor is a fundamental requirement to understanding how the crystals grow¹⁸, and how the composition of the material can drastically affect the resulting morphology¹⁹, the ability to localise their deposition, or indeed write or pattern them onto surfaces.

Since NPs and other nanoscale objects introduced into polymers can demix and coarsen into clusters through collective nucleation processes such as spinodal clustering^{20–22}, they also prevent polymer dewetting from a surface^{23,24}. These two factors inspired the hypothesis that shape controlled crystals from nanoscale to micron sizes could be controllably grown, positioned and the growth mechanisms monitored, directly on surfaces. Defining the role of nanoscale crystals and their influence on the crystallization of their coarsening or assembly,



is a major challenge for materials science²⁵. The surface-growth capability allows for growth pathways to be tracked in real-time using standard surface microscopies amenable to many laboratories. The formation of patterned nanoscale metallic structures by solid state dewetting²⁶ has proven useful for array formation and in porosity development^{27,28}, but is often limited thin metal films in the first instance, where complex shaped crystals are not possible, and the metal content and resulting composite structure cannot be tuned as it can be with metal-polymer mixtures.

Results

We designed cyclic polymer and trimer-based complexes incorporating Au, Ag, Pd, and Re at the molecular level to allow pyrolytic demixing of physical mixtures of an organometallic derivative or metal salt, and polypyro-, and spirocyclic polyphosphazene (see Supplementary material). $[\text{N}_3\text{P}_3(\text{O}_2\text{C}_{12}\text{H}_8)_3]$ or $[\text{NP}(\text{O}_2\text{C}_{12}\text{H}_8)_2]_n$ ($\text{O}_2\text{C}_{12}\text{H}_8 = 2,2'$ -dioxy-1,1'-biphenyl) (Supplementary materials, Fig. S1) were synthesized and prepared that have λ^5 -dioxydiaryl groups in the repeating units (polyspirophosphazenes). The metallopolymer forms a bottom-up, spin-cast precursor; the metal is coordinated at a predefined position within the macromolecule. The pyrolytic approach and chemical decomposition processes these polymers undergo are summarized in Supplementary materials, Figs. S1–3.

For Au, the overall process leading to complex crystal shapes through demixing is summarized in Fig. 1. The cleaved metal atoms from early stage decomposition form NPs within the organic matrix (see Supplementary material, Fig. S4). Initial nucleation dewetting of the composite metallopolymer (Fig. 1A1), leads to the beginning of pinhole void formation (Fig. 1A2), whose complete beading is suppressed by the inclusion of metallic NPs²⁹, observed by STEM to be distributed within a labyrinthine (spinodal-like) network of the carbonizing polymer with a dominant length scale and interconnectivity

between pinholes (Figs. 1B1, 1B2 and details in Supplementary material, Figs. S4,5). The pinhole density becomes constant after solidification of the carbonized polymer matter.

Heterogeneous nucleation in the early stages (with spinodal character, Fig. 1A2) occurs where the metallopolymer is liquid for a brief time above T_g , allows mobile NPs to migrate solely toward the pinned rims of the pinholes, eventually ripening to a platelet seed (Fig. 1B3). For all processes in this work, the remarkable finding is that the pinholes form miniature reactors where crystallization and growth uniquely occurs. The process of spatially pinned seed formation and incubation is trackable using AFM, where in Fig. 1C, we observe the clustering²⁰ of NPs and the formation of 2D platelet seeds within the pinholes. We find that the subsequent crystallization of Platonic and complex shaped crystals uniquely from these pinholes (Figs. 1A3 and 1D), including geometrically perfect tetrahedra, decahedra and even single crystal metallic truncated icosahedra. A similar pathway leading to specific crystal shapes is also demonstrated for Ag, Pd and Re (see Supplementary material, Fig. S6) using appropriately design macromolecular structures mixed with the corresponding metal salts.

Figure 1E demonstrates that halting of the pyrolysis indicates that the pinhole density is always greater than the density of crystals that eventual grow within them, until the vast majority of pinhole growth sites contains crystals. In this case, sufficient Au is present within the matrix to fill all available pinhole sites that form as a tessellation in the solidified matrix; the percentage of crystal-filled pinholes increases from 72% (at the stage where solidification is complete at $\sim 500^\circ$, to $< 93\%$ after full pyrolysis and annealing. Imaging after oxygen plasma etch removal of remnant organic matter confirms that the undulating features are not solely due to clusters forming under the polymer but from the instability throughout the matrix. The surface buckling is not due to spatial variations in surface tension during the brief period the metallopolymer is liquefied and importantly, the films never dewet the substrate. Some definitive features

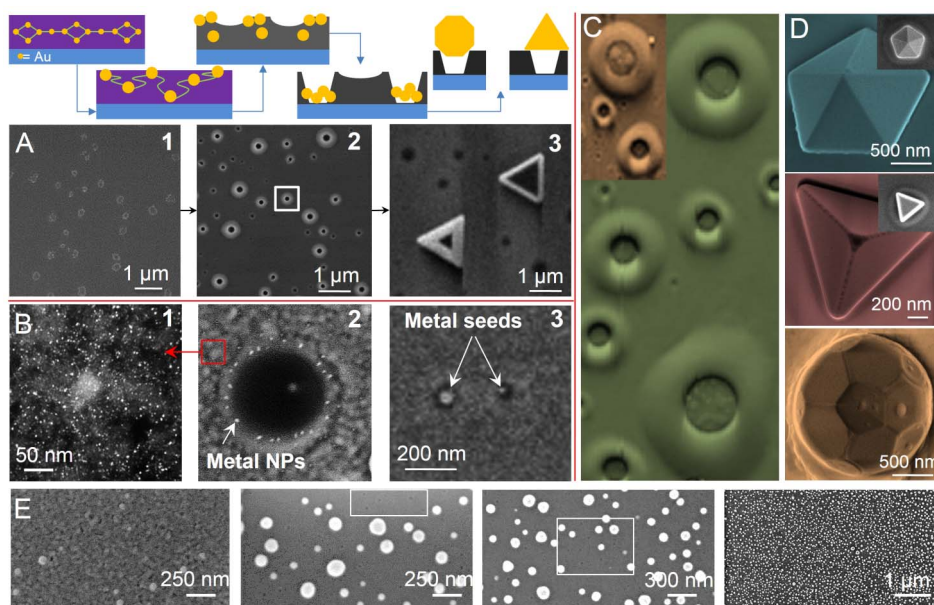


Figure 1 | Tracked mechanism of solid state NP and complex crystal growth using Au. (A): (1–3) Pinhole formation in a solidifying metallopolymer during heating, forming a fixed array of pinholes leading to predefined density of shaped Au crystals. (B): (1) HAADF TEM images of gold NPs formed in the early decomposition stages. The lighter background features are the polymer matrix, bright points are the NPs. (2–3) Aggregating NPs migrate in-plane and from within the matrix to the pinhole acting as a nucleation point. Seeds form from Au NPs uniquely within pinholes. (C): AFM images of early stage growth where the nucleation of a crystal through NP coarsening within pinholes in the polymer is observed. While aggregation occurs at the nucleation pinhole, a single 2D crystal is first formed in all cases. (D): geometrically perfect micron-sized decahedron, tetrahedron and truncated icosahedron of single crystal gold grown in the solid state. (E): series of SEM images at frozen stages of crystal growth of Au crystals. The spatial density follows the pattern of pinholes on the surface once the seed is nucleated within a pinhole. Empty growth sites are shown in the outlined regions.



are observed during the crystal growth evolution. The nearest neighbor distance is typically related to the density of pinholes, and the density of pinholes defines the number of incubated crystals. This observation occurs with sufficient gold content in the macromolecular precursors to feed the crystal growth. As will be explained below, crystal growth depletes the region around the crystal of Au NPs, and thus limits the development (density) and size of next-nearest neighbor crystals and reduces the density, leaving empty pinholes (Fig. 1E). This phenomenon is also observed for Pd and Ag NP and crystal growth systems reported here.

These crystals ripen from the pinholes uniquely, and EDX, XRD and XPS for these systems (see Supplementary material, Figs. S7–9) confirm the phase-pure, single crystal metallic composition of each metal within the matrix without surface bound contaminants of growth-influencing organics or carbon residues from the pyrolysis, as seen in HRTEM analysis of high index facet surfaces (see Supplementary material, Fig. S10). The resulting crystals formed are free from a carbon coating and with a defined areal density.

Detailed AFM examination shows a consistent link (for a given metal:organic ratio) between the thickness of the deposit and the density of pinholes (as expected) but also the *shape* of the resulting crystals; thinnest deposits (60–150 nm) give tetrahedral growth (see Fig. 2), thickest deposits ($> 3 \mu\text{m}$) resulted in pathways to metallic truncated icosahedral crystal growth.

As we show in Fig. S7 and Fig. 2, cuboctahedra and tetrahedra are tracked at various stages of 3D growth. The crystal can be grown on almost any surface, or any shaped surface and the crystal shape evolution is maintained from nanoscale NPs up to micron scale crystals. While solution based synthesis offer mass production for a given size dispersion³⁰, it approach requires additional methods often utilizing surface charge, potential gradients, or other deposition methods such as direct writing, droplet moulding³¹, and parallel

printing to control position and location of individual or assembled materials. Pinning the entire crystal growth at a defined location also allows the growth method to be more amenable followed.

We investigated the growth evolution of the crystal in detail (in terms of crystal growth and symmetry rather than ripening or coarsening kinetic of the source NPs) and several pathways are outlined in Fig. 2 for Au; the types of crystals found for Re, Pd and Ag are shown in Supplementary material, Fig. S6 for comparison. The ripening steps of the tetrahedral Au microcrystals can be monitored from nanoscale clipped triangular platelets³² (initial growth) to full tetrahedra (final structure), shown in Fig. 2A(1-7). As in solution systems, the tetrahedra evolve asymmetrically, where the edge length is first defined by forming a vertex-clipped 2D platelet delineated by dominant $\{111\}$ ⁴ facets. Here, this shape maintains the same geometry from nm sizes through to micron scale as a 2D platelet due to being pinned at its incubation pinhole (NP nucleation and crystallization) site. The platelet then evolves to three-fold rotational symmetry to a triangle with fully formed vertices, but always maintains its initial 2D footprint area (even when, by this method, the incubation pinhole is larger than neighboring pinholes). Subsequent growth after the vertices are defined, upfills the structure until a geometrically perfect tetrahedron is formed^{2,12}. The net effect contributes to the growth of clipped 2D platelets, observed many times in solution based approaches from nm to micron scale before forming the triangular platelet for continued growth (Fig. 1 and S7).

On the nanoscale, penta-twinned seed NPs are found to grow to nanoscale icosahedra, but subsequently evolve to micro-scale decahedra (pathway Fig. 2B) as was recently suggested using heterometallic plasmonic labelling experiments on the nanoscale⁴. This observation confirms our hypothesis that the crystals fed from laterally mobile NPs evolve until all low energy $\{111\}$ facets are dominant. Importantly, the method of tracking ripening growth allows a

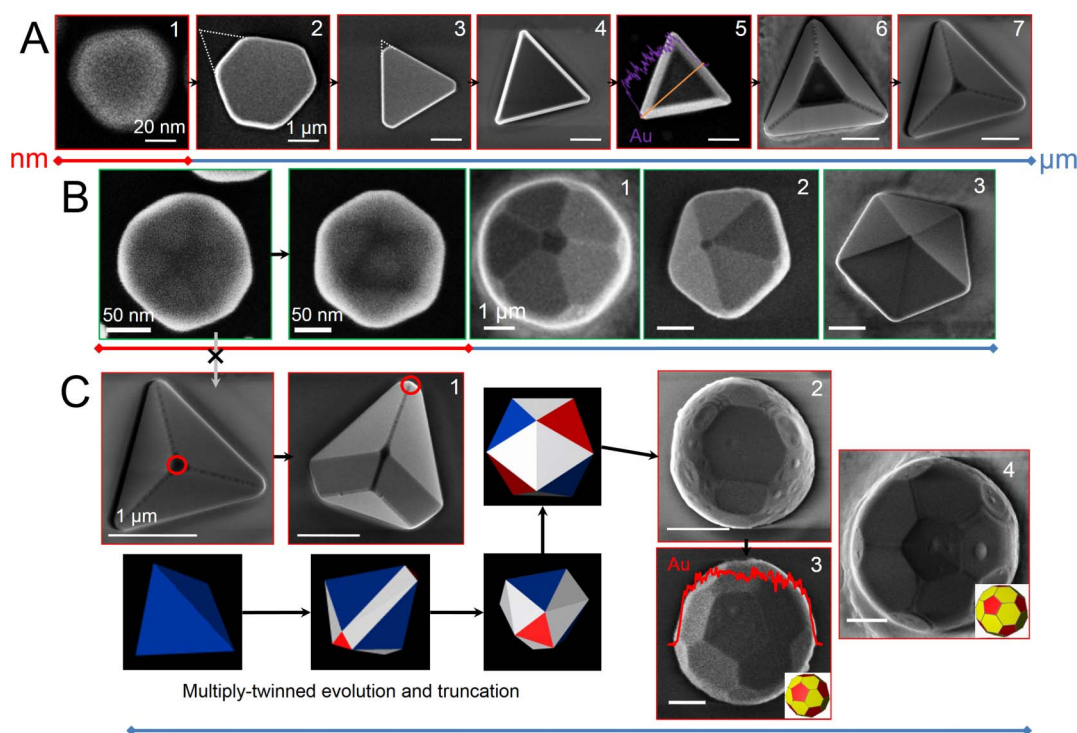


Figure 2 | Tracking solid state crystal growth. (A1-7) The evolution of clipped triangular platelets and vertex formation to form a complete triangular platelet; subsequent growth results in a geometrically precise tetrahedron. (B) Penta-twinned NP that evolves to 20-fold icosahedron on the nanoscale. (B1-3) The evolution of icosahedra to micron scale decahedra by anisotropic growth of clipped decahedra with subsequent outfilling from a pinned substrate position. (C1-4) Evolution of tetrahedral on the micron scale to truncated bitetrahedra and eventually (via schematic on the left) to truncated icosahedral crystal form. Unmarked scale bars = 1 μm .



true assessment of the shape evolution from the feedstock of metal atoms and nanoparticles that move towards the growth site in the dewetted, solidified polymer, without the complication of attachment of separately formed shapes. For example, oriented attachment of two tetrahedra to form a bitetrahedra would incorrectly describe the shape evolution process, which is difficult to monitor and control in solution syntheses for a single growing crystal.

In contrast to recent findings⁴ however, the penta-twinned NPs during crystallization are not found to evolve to tetrahedra (pathway B to C, Fig. 2). We consistently find that tetrahedra are observed to grow via the addition of extra twin planes by a different pathway – the primary difference compared to solid state thin film dewetting or all solution syntheses is the pinning of the crystallization site. Decahedra are not observed to evolve to 20-fold twinned icosahedra; tetrahedra on the micron scale, by continued preferential ripening from NPs within the spinodally decomposing metallopolymer, evolve by the addition of pairs of new triangles in place of the original six edges of the tetrahedra^{13,33}. The structure then evolves to non-uniform truncated icosahedra and then to perfect truncated icosahedral fullerene shapes (pathway C1–C4), a pathway not previously seen for any size of metallic or other inorganic crystal, and its growth was tracked from a 2D nanoscale platelet seed (Fig. 2A1–7 + C1–4) in the solid state. In all cases where the metastable metallopolymer thickness results in specific shapes (Fig. 1), micron sized shapes grow from specific nanoscale shapes, beyond thermodynamic limitations of solution growth.

Tracking the growth mechanism allows and shape evolution pathways offers the potential to create a variety of new structures for materials that can phase separate in this manner, including a range of organometallic precursors, and possibly others unobtainable by standard solution-based methods. We investigated the possibility of using nucleation and phase demixing/spinodal clustering, to create free-standing and spin-cast film composites for catalysis. Demixing and spinodal-type processes are dependent on many factors, such as the NP loading, thickness, m.w. and viscosity etc. Due to chemical changes in the polymer during pyrolysis in air, *i.e.* the carbon support (see Supplementary material, Figs. S2,3), its solidification, and the ripening of NPs (larger NP sizes with greater interparticle spacing), these factors dynamically change. Scaffolds for nanoparticles have been previously detailed for colloidal NP systems, and protocols for important dispersion of nano-objects in supports are well established. We find that our method allows for a definable switch in morphology. When the mixture ratio is 1:10 (larger polymer fraction), we find that mildly faceted NPs follow the surface pattern of the pinholes, but on a thick carbon residue (Fig. 3A1). For thicker eventual deposits, the NPs are found to be smaller in size but do not develop faceting and are spherical (Fig. 3A2); for the thickest (up to 30 μm , near-bulk) deposits we find NP-embedded carbon supports for all metals examined. For Re (Fig. 3B), high-index faceted NPs (shown in more detail in Supplementary material, Fig. S10) form within a carbon support, where it characteristically forms via a layered growth process as the crystal emerges from the pinhole. Re crystals are unique in that they do not form defined polyhedral shapes on the micron scale. In the Supplementary material, Fig. S6, the larger crystal of Re form a layered structure, where the layers clearly form in a nautilus-like fashion from crystallization of coalescing NPs with lower mobility. The crystals rotate as they grow from the pinholes giving the characteristic high surface area, layered morphology. Analogous to the uniqueness of the Re crystallization by comparison to Ag, Au and Pd, the corresponding early stage NPs shown in Fig. 3C, are high index faceted NPs with a narrow size distribution centered at a typical NP size of ~ 3 nm (Fig. 3D). XPS measurements confirm that the metallic NPs are freely accessible in the porous support and are not coated with carbon or other contaminants. The method allows direct infiltration of NPs with a carbon host, which is made porous through the formation of pinhole

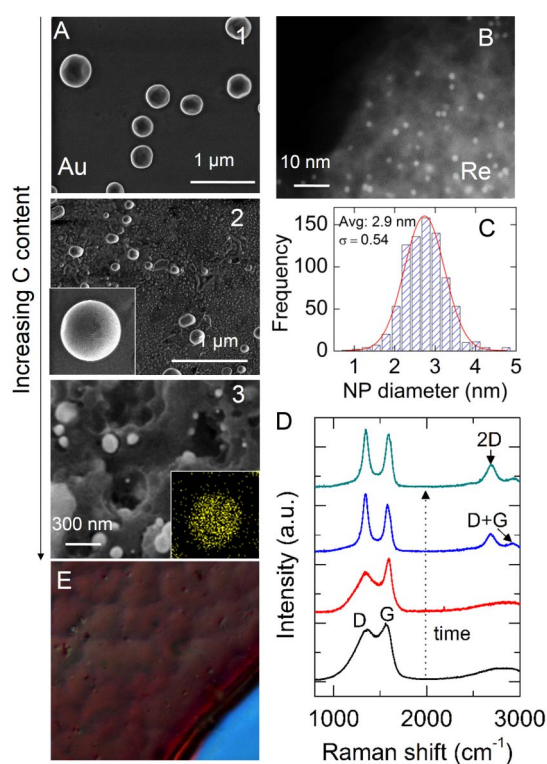


Figure 3 | Tuning crystal size and forming NP-loaded layered graphitic composites. (A) SEM images of pseudo-spherical, partially faceted Au crystals formed from a (1) 3:1 trimer:gold mixture (2) 5:1 mixture ratio and (3) 10:1 NP($\text{O}_2\text{C}_{12}\text{H}_8$)₃/AuCl(PPh_3) ratio; the inset EDX map confirms phase pure Au. As the carbon content increases, so does the deposit thickness and the propensity for higher internal crystal density, with decreasing NP size (less Au). (B) Direct formation of high-index facet Re NPs within a carbon support. (C) Size dispersion of high index Re NPs within the graphitic matrix. (D) Raman scattering of the surface carbon deposit confirming conversion to graphite where D and G bands and harmonics related to crystalline defective graphite are tracked in time. (E) A ~ 1 mm thick deposit on SiO_2 , functionalized using Rhodamine (B) dye to show the morphology of the NP-loaded film.

incubation sites for the growing metallic crystals. The formation of NO_2 , CO and CO_2 gases (see Supplementary material, Fig. S2 and S3), is also likely to contribute to the internal porosity of the carbon support.

Raman scattering investigations (Fig. 3D) of the carbonization at several stages shows the emergence of convoluted scattered phonon processes as definitive D and G-bands, describing a mixture of 2D and 3D graphite eventually forming of a layered 3D graphitic foam³⁴ (analysed in Supplementary material, Fig. S11) which is specifically due to the solid carbonaceous cyclomatrix formation (see Supplementary material, Fig. S12). The spectra evolve during pyrolysis to fingerprints of layered graphite, with remarkable similarity to layered graphene flakes with ‘defective’ curvature³⁵. Using AFM, we find that the thickness significantly increases with higher carbon content, forming a graphitic 3D foam, from ~ 30 μm to over 1 mm in thickness on a surface, loaded with NPs (Fig. 3A3). In this case, subject to a specific further investigation, the overarching mechanism allows for a defined NP loading density based on the structure of the metallopolymer and its phase demixing. This provides a tunable, single-step alternative to NP infiltration techniques and avoids agglomeration while maximizing spatial dispersion due to the structure and decomposition characteristics of the metallopolymer. During thermal decomposition, the mixture ratios that provide such composite

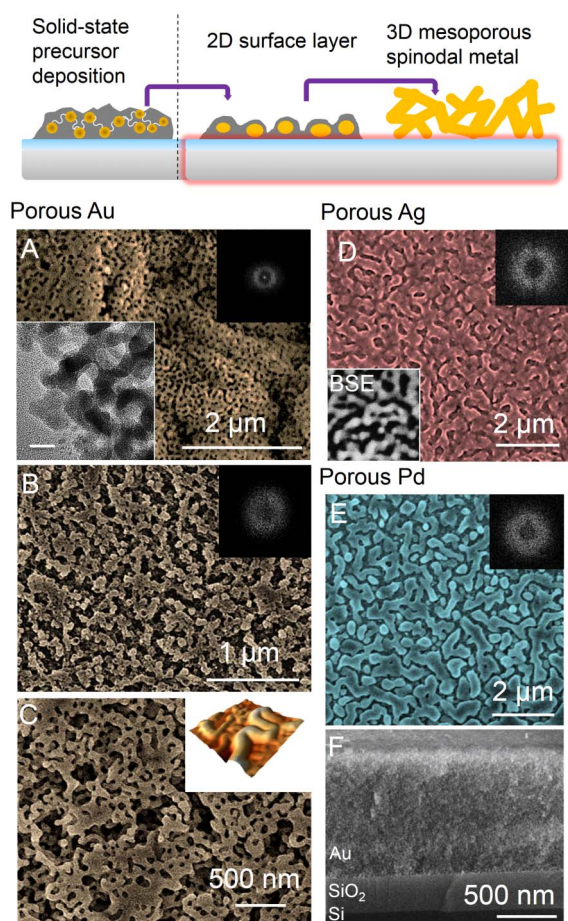


Figure 4 | 2D and 3D porous metal film crystallization.

(A–C) Hierarchically porous Au formed by a spinodal decomposition of a $[\text{NP}(\text{O}_2\text{C}_{12}\text{H}_8)]_n/\text{AuCl}(\text{PPh}_3)$ mixture with high Au content. HRTEM (inset) confirms the mesoporous metal structure. The smallest instability or feature wavelength occurs for the thickest films. (D), (E) Porous Ag and Pd thin films formed without dealloying, confirmed by back-scattered secondary electron imaging (inset) and (F), thick porous Au layer with consistent 3D inter-feature separation, cast on oxidized Si wafer. The insets are radially average FFTs of the porous metals confirming constant feature-feature separation in all directions.

structure can have the size and density of NPs tuned. Short times provide dense, small NPs and longer heating times provide fewer, larger crystals. Figure 3E shows how a thin film porous carbon film that is interspersed with metallic crystals can be uniformly dye-functionalized.

Finally, we show that precursors with high metal content allow a facile one step route to pure porous metals and foams with a spinodal, 3D disordered gyroidal morphology (Fig. 4), either as thick, 3D porous films, or as 2D porous metal coatings. Porous metals are an important class of materials used in ultra-sensitive SERS substrates³⁶ and have unique properties such as high stiffness, low density, gas permeability and thermal conductivity for catalysis, hydrogen storage and acoustic insulation. Preparative methods for metal foams to date most commonly involve de-alloying of bimetallic Au_xAg_y ^{36,37}. Recent methods have achieved some control in porous metal formation by spinodal and melt-induced dewetting of metallic thin films²⁷. Controlling the distance between metallic features in stochastically dealloyed foams has been theoretically examined, but experimental verification of dealloying is limited for other metals; tuning the length scale between high aspect ratio features (proximity of sharp edges) is paramount for the enormous application possibilities of

these materials. In SERS, the control of inter-feature width and curvature (edge definition) is crucial for maximal EM-field enhancement³⁸. Maintaining a given porosity and porous structure from 2D to 3D, has not been achieved for Au or other metals, even though a very wide variety of metals can be dewetted in nanoscale features through localized heating²⁷ or ion bombardment³⁹. This capability is useful in cases where dealloying of phases other than Au_xAg_y is desirable, but not possible without a good contrast in standard reduction potentials for the alloy components. By changing the metal:polymer ratio to a high metal content (see Supplementary material), the decomposition mechanism allows the spinodal-like patterning to occur for all metals examined, as confirmed through high resolution electron and surface probe microscopies in Fig. 4. The bottom up growth of the porous structure method differs from heating of thin metallic films, which is a top down dewetting process which inherent limitations in the degree of porosity that is possible. The formation of the characteristic percolating lateral topography with a 3D labyrinthine overall morphology²⁹, initiated at the substrate interface, then maintains a characteristic and constant feature-feature distance in the metallic mesoporous morphology in 3D, even for layers that are several microns thick (Fig. 4F). In Fig. 4(A–E), the rings in Fourier space do not strictly refer to the formation mechanism, although they can often be used as signatures of spinodal decomposition in systems where this has been established; here, they confirm the random orientation and the degree of consistency of the inter-feature distances in each case, for both 2D films and thick, 3D porous layers, without adverse effects on SERS from remnant Ag often present in dealloyed materials⁴⁰.

Discussion

Consistent with nucleation and demixing, all the remaining polymer between the pinholes in the thermalized deposits on surfaces becomes depleted of NPs as the lateral coarsening-feeding of the crystal growth continues; crystal egress continues ‘layer-by-layer’ from ripening NPs within the polymer structure, and also from NPs located on and near the surface. The younger ripening seed crystals form with good monodispersity prior to shape evolution, and their density is commensurate with metallopolymer thickness due to the uniform metallic content in the precursors, a denser dispersion of NPs (of similar size and shape) is characteristically found from thicker deposits (see Supplementary material, Fig. S13)²⁸. The mechanism of pinhole formation is progressive and as the carbonaceous materials solidifies and hardens the surrounding materials, the resulting crystals have a variable size and degree of development. The preference for Au NP clustering indicates a strong (preferential) interparticle interaction⁴¹, where small seeds coalesce with a spatially pinned growing seed (in the pinholes) driven by phase separation rather than just coalescence²⁰. This coarsening in the solid state is not likely to be dominantly controlled by thin-film 2D confinement as was found for aggregation of inclusions in simple PS thin films. The NPs also diffuse faster than aggregates of NPs tethered by polymer chains⁴², which do not ripen to a single geometrical crystal.

It should be noted that the final diameters of the pinholes (crystal growth ‘reactor’ sites) remain unchanged after carbonization solidification. The pinholes as nucleation points become pinned, essentially defining where crystal growth will only occur. In related solid state approaches such as dewetting of thin metallic films, break up to form NPs or meandering porous networks does not typically allow a reforming of a defined geometrical crystal shapes. Here, metal atoms migrate by spinodal clustering to the seeding crystal in a manner that preserves perfect crystal symmetry without changing the geometry during ripening and growth. Analysis of NP density from STEM images confirms a dominant 2D phase separation process (see Supplementary material, Figs. S4 and S13); for thicker films, NPs can migrate from within the decomposing mixture to the nucleation site (pinholes open the deposit from air to substrate). Each final



shape of crystal maintains a near-equal volume and edge length (see Supplementary material, Fig. S7) in spite of nucleation and growth being progressive rather than instantaneous and coupled. Consistently, all equivalent shapes finish with similar outer dimensions and overall volume.

In solution, large jumps in crystal size are typically accompanied by evolution to thermodynamically lower energy shapes, such as spheres. The energy minimization has been demonstrated experimentally and theoretically¹³ for nanoscale systems in solution. These calculations predicted a size threshold where the energy barrier for structural change becomes too great. The solid state decomposition of a molecular level building block metallopolymer undergoing phase demixing allows each crystal shape to evolve and maintain its complex geometry over a range of length scales – the shape evolution pathway is trackable. The density of pinholes is defined by the mixture ratio and molecular weights, and this ultimately defines the spatial density for a given crystal shape, for any stage of the shape evolution, which can be halted by quench cooling on a heat sink. Figure 1 showed stages of shape evolution and spatial density for triangular platelets that eventually grow to tetrahedra (Fig. 2), where the pinhole density is defined prior to the final crystal density (for sufficient metal content).

The porous metals form by the combination of a spinodal-type instability but dominantly, a crystallization of a high NP coarsening, mimicking a spinodally decomposed polymer with metal NP inclusions⁴³. The ‘inverted’ porous metal formation occurs in $\text{N}_3\text{P}_3(\text{O}_2\text{C}_{12}\text{H}_8)_3/\text{AuCl}(\text{PPh}_3)$ and $[\text{NP}(\text{O}_2\text{C}_{12}\text{H}_8)]_n/\text{AuCl}(\text{PPh}_3)$ mixtures, because a strong Au-arene interaction (between the $\text{AuCl}(\text{PPh}_3)$ molecules and the biphenyl rings) allows regular ordering of the Au centers along the $\text{NP}(\text{O}_2\text{C}_{12}\text{H}_8)$ groups of the polymer chains, or around the cyclic molecules of trimers. The NP association length however, is difficult to follow inside a carbon support during formation. The instability development and porous metal topology could allow a wide range of functional metallic and oxide porous materials. The definition of the porosity and equidistance metal-metal distances in porous metals is linked definitively to the molecular structure of the precursor and the demixing/decomposition mechanism is likely to be adaptable to many metal-containing inorganic and metallic precursors. Defined deposition and porosity in porous Pd for example, as a pure metal or as a NP-containing composite augers well for catalytic application used in Li- O_2 batteries⁴⁴ and Suzuki, Heck and Negishi reactions, and gas sensing as pertinent examples. The dynamics of high metal loading and crystallization might also provide opportunities for periodic and complex, ordered porous metallic structure formation.

Fundamentally, the observation of competitive demixing/dewetting of the polymer phase during decomposition the kinetics of crystallization from mobile NPs into complex shapes crystals and metals with tunable porosity will need to be examined in further detail. Some features have been established: the mobile NPs form specific crystals (when the minimal gold content and thickness of the deposit are defined) while the polymeric phase is liquid, since negligible Au content is found in the surrounding polymer phase after carbonization (except for the mixture ratios that form NP-loaded carbon composites). NP association on and within polymers has been tested using Avrami and related kinetics, while nucleation and spinodal decomposition mechanisms (material independent) can accurately describe the pinhole formation and labyrinthine structure formation in simpler systems. Future work might identify the correct mechanism involved in the competitive scenario shown here for greater composition and structural control of the resulting materials and patterns, particularly with progressively increasing viscosity (which occurs with an increase in temperature, but due to solidification) of the material during crystal growth.

This bottom-up single-step approach for molecular level metallopolymer building blocks that crystallize into a variety of defined

structures and shapes provides a single step growth method without ligands or surfactants in solution to influence growth or shape. The association of NPs during phase demixing and the decomposition of the polymeric phases, which can be monitored, ultimately define the resulting structures into complex polyhedral crystals, metal-loaded porous carbon supports or porous metals. The method allows almost all important polymorphs of metallic crystals to form including an ability to monitor and delineate the growth process. Additionally, the growth pathways can be observed at all stages, where lateral demixing and subsequent ripening process give a well-defined crystal through a trackable shape evolution pathway. The areal density of the crystals depends on the thickness of the deposit, the structure of the macromolecules, the metal loading and the competitive interplay between physical and chemical decomposition pathways allowing a transition between surface-bound individual crystals, carbon supported high index NPs, and tunable porosity metals⁴⁵. This is made possible by demixing of a metal-containing macromolecular complex and co-processes of NP seed formation and incubated crystal growth in a graphitic matrix. When other materials are chosen, the approach has potential for multifunctional materials, liquid and water-free inorganic crystal synthesis for charge storage applications, plasmonics and SERS involving large scale porous metal films on any type of surface, photovoltaics⁴⁶, and sensing when transition metals are used to form patterned oxides that can be deposited or even written using AFM onto surfaces. Scope also exists for supracrystallization of various crystal sub-units into complex functional assemblies which can be readily observed during growth. For example, porous loaded carbons improved by further development may be applied to catalytic composites using small NP loaded carbons for conversion processes in catalysis and energy storage conversion processes where the placement NPs into support matrices without agglomeration and shape changes is possible during synthesis. This approach can be readily extended to a very wide range of transition metal oxide, metalloid and semiconductor crystal growth, composite formation and porous assemblies.

Methods

Solvents used were dried a purified using standard procedures. The starting materials $[\text{NP}(\text{O}_2\text{C}_{12}\text{H}_8)]_n$ (with a m.w. of 600,000) and $[\text{N}_3\text{P}_3(\text{O}_2\text{C}_{12}\text{H}_8)_3]$ (1) were prepared using the reported methods. The mixture complexes were prepared in high yield (96%) and evaporating the solvent. The purity of the product was verified by³¹ P-NMR. Details on the mixtures, and their composition are as follows:

Preparation of the mixtures. $\text{AuCl}(\text{PPh}_3)/[\text{NP}(\text{O}_2\text{C}_{12}\text{H}_8)]_n$. The $\text{AuCl}(\text{PPh}_3)$ complex was prepared in high yield by adding AuCl (Aldrich) to a dichloromethane solution of PPh_3 (1 : 1 molar ratio) and evaporating the solvent. Table 1 summarises the experimental conditions for the preparation of the mixtures.

$\text{AgPPh}_3[\text{CF}_3\text{SO}_3]/[\text{NP}(\text{O}_2\text{C}_{12}\text{H}_8)]_3$. $\text{AgPPh}_3[\text{CF}_3\text{SO}_3]$ (0.3795 g, 9.5×10^{-4} mmol) and $[\text{NP}(\text{O}_2\text{C}_{12}\text{H}_8)]_3$ (0.5130 g, 7.46×10^{-4} mmol) for a molar relationship 1 : 1; $\text{AgPPh}_3[\text{CF}_3\text{SO}_3]$ (0.074 g, 1.86×10^{-4} mmol) and $[\text{NP}(\text{O}_2\text{C}_{12}\text{H}_8)]_3$ (0.4234 g, 6.16×10^{-4} mmol) for a molar relationship 1 : 5 and $\text{AgPPh}_3[\text{CF}_3\text{SO}_3]$ (0.0594 g, 1.5×10^{-3} mmol) and $[\text{NP}(\text{O}_2\text{C}_{12}\text{H}_8)]_3$ (0.4064 g, 5.9×10^{-4} mmol) for a molar relationship 1 : 10, were stirred in a CH_2Cl_2 solution at room temperature for 24 h. After this the solvent was eliminated under reduced pressure and the solid dried under a vacuum at room temperature.

Table 1 | Summary of the experimental conditions for the preparation of the mixtures (n = 3 or polymer)

Mixture	Polymer/Au	Trimer/Au	g of Au	g of Trimer	g of Polymer
1	3 : 1 ^a		0.11		0.15
2		3 : 1 ^c	0.004	0.017	
3		5 : 1 ^c	0.0858	0.0238	
4		10 : 1 ^c	0.027	0.3865	

^aFilm;

^bPower method.



$PdCl_2/[NP(O_2C_{12}H_8)]_3$. The respective molar mixture of Palladium chloride (0.1 g, 0.56 mmol for the 1:1 ratio mixture) and (0.14 g, 0.789 mmol for the 1:5 ratio mixture) and the trimer $[NP(O_2C_{12}H_8)]_3$ (0.4 g, 0.58 mmol for the 1:1 ratio mixture and 1.94 g, 2.82 mmol for the 1:5 ratio mixture) were dissolved in CH_2Cl_2 , stirred for 24 hours and evaporated to dryness under vacuum at room temperature.

$K[ReO_4]/[NP(O_2C_{12}H_8)]_3$. The mixtures of $K[ReO_4]$ (0.1 g, 0.354 mmol) and the cyclotriphosphazene $[NP(O_2C_{12}H_8)]_3$ (1.19 g, 1.73 mmol) for the 1:5 molar ratio and of $K[ReO_4]$ (0.03 g, 0.103 mmol) and $[NP(O_2C_{12}H_8)]_3$ (0.7 g, 1.018 mmol) for the 1:10 molar ratio, were dissolved in dichloromethane, stirred for 24 hours and evaporated under vacuum until dry.

Powder. The respective molar mixtures above are each dissolved in THF, stirred for 24 h and evaporated to complete dryness in a vacuum at room temperature.

Deposition of the mixtures on Si or SiO_2 . A drop of CH_2Cl_2 solution containing the mixtures (solutions/suspensions in the range 1×10^{-3} – 5×10^{-4} g/mL) was cast over either a silicon or oxidized silicon surface and the solvent evaporated. The Si or SiO_2 wafer (with 400 nm of thermally grown oxide) was subsequently pyrolyzed (see Supplementary materials, Fig. S1) at 800 °C using a predefined temperature program (Daihan oven model FHP-12) where the polymer samples were heated at a rate of 10 °C min⁻¹ from room temperature to 800 °C under a constant air flow of 120 mL min⁻¹ and subsequently annealed for 2 h. The resulting depositions give a uniform areal coverage for each mixture.

Analytical techniques. X-ray diffraction (XRD) was carried out at room temperature on a Siemens D-5000 diffractometer with θ -2 θ geometry. The XRD data was collected using Cu-K α radiation (40 kV and 30 mA). Scanning electron microscopy (SEM) and energy dispersive X-ray analysis (EDX) were acquired with a JEOL 5410 SEM with a NORAN Instrument micro-probe transmission microscope and with a Hitachi SU-70 FESEM operating at 10 kV equipped with an Oxford Instruments X-max 50 mm² solid-state EDX detector for elemental line scans and mapping. AFM measurements were acquired with a Veeco Instruments Enviroscope operating in intermittent contact mode. X-ray photoelectron spectroscopy (XPS) was acquired for deposits on Si and SiO_2 surfaces in normal emission geometry. A VG CLAM 2 spectrometer with an Al K α X-ray source (1486.6 eV), operating at 250 W, were used several centimeters from the samples. The spectra were normalized to the total electron yield to correct for small differences in sample positions and X-ray source intensities. The resulting spectra were fitted by using a Shirley-type background and symmetric Voigt functions with variable Gauss and Lorentz contributions.

Image analysis of feature topology. AFM and optical microscopy were used for analysis of patterns, topologies and morphologies of the NP coarsening and overall crystallization process. For *in-situ* examination of crystal growth and cluster size formation, optical microscopy data and AFM data was acquired during pyrolysis up to the spinodal feature development stage. Both techniques were used to follow the variation of the in-plane morphology, *i.e.* the direction of NP migration and feeding of crystal growth and patterning. Height variations of patterns and crystal were obtained by AFM and compared to SEM.

Structure factors used for pattern determination and crystal/pinhole relative positions on films were acquired by thresholding digital images and obtaining radially averaged fast Fourier transforms (FFT). The maximum intensity of the structure factor $S(k)$ from FFTs gives the wavelength of surface morphology in the case of spinodal-like pattern formation, where the wavelength $\lambda = 2\pi/k$. Random distributions of nanoparticles and morphologies without any definitive wavelength in position within the morphology give a decaying intensity from the maximum intensity (000) central mode. Nanoparticle and crystal coverage within decomposed films from SEM and high resolution TEM images were determined using ImageJ analysis software for particle size and spatial distributions, accounting for shape anisotropy. NP cluster densities were measured using optical microscopy.

1. Langille, M. R., Personick, M. L., Zhang, J. & Mirkin, C. A. Bottom-Up Synthesis of Gold Octahedra with Tailorable Hollow Features. *J. Am. Chem. Soc.* **133**, 10414–10417 (2011).
2. Tao, A. R., Habas, S. & Yang, P. D. Shape Control of Colloidal Metal Nanocrystals. *Small* **4**, 310–325 (2008).
3. Sau, T. K. & Rogach, A. L. *Complex shaped metal nanoparticles – Bottom-up syntheses and applications.* (Wiley-VCH, 2012).
4. Langille, M. R., Zhang, J., Personick, M. L., Li, S. & Mirkin, C. A. Stepwise Evolution of Spherical Seeds into 20-Fold Twinned Icosahedra. *Science* **337**, 954–957 (2012).
5. Langille, M. R., Personick, M. L., Zhang, J. & Mirkin, C. A. Defining rules for the shape evolution of gold nanoparticles. *J. Am. Chem. Soc.* **134**, 14542–14554 (2012).
6. Li, Y. & Somorjai, G. A. Nanoscale Advances in Catalysis and Energy Applications. *Nano Lett.* **10**, 2289–2295 (2010).
7. Tian, N., Zhou, Z.-Y., Sun, S.-G., Ding, Y. & Wang, Z. L. Synthesis of Tetrahedral Platinum Nanocrystals with High-Index Facets and High Electro-Oxidation Activity. *Science* **316**, 732–735 (2007).

8. Dreaden, E., Huang, X., Alkilany, A. M., Murphy, C. J. & El-Sayed, M. A. The Golden Age: Gold Nanoparticles for Biomedicine. *Chem. Soc. Rev.* **41**, 2740–2779 (2012).
9. Cao, Y. C., Jin, R. & Mirkin, C. A. Nanoparticles with Raman spectroscopic fingerprints for DNA and RNA detection. *Science* **297**, 1536–1540 (2002).
10. Anker, J. N. *et al.* Biosensing with plasmonic nanosensors. *Nat. Mater.* **7**, 442–453 (2008).
11. Sau, T. K. & Murphy, C. J. Room Temperature, High-Yield Synthesis of Multiple Shapes of Gold Nanoparticles in Aqueous Solution. *J. Am. Chem. Soc.* **126**, 8648–8649 (2004).
12. Sun, Y. G. & Xia, Y. N. Shape-controlled synthesis of gold and silver nanoparticles. *Science* **298**, 2176–2179 (2002).
13. Elechiguerra, J. L., Reyes-Gasca, J. & Yacaman, M. J. The role of twinning in shape evolution of anisotropic noble metal nanostructures. *J. Mater. Chem.* **16**, 3906–3919 (2006).
14. Wang, X., Zhuang, J., Peng, Q. & Li, Y. A general strategy for nanocrystal synthesis. *Nature* **437**, 121–124 (2005).
15. Yuk, J. M. *et al.* High-Resolution EM of Colloidal Nanocrystal Growth Using Graphene Liquid Cells. *Science* **336**, 61–64 (2012).
16. Ma, Y. *et al.* Seed-Mediated Synthesis of Truncated Gold Decahedrons with a AuCl/Oleylamine Complex as Precursor. *Adv. Mater.* **22**, 1930–1934 (2010).
17. Yu, Y., Zhang, Q., Xie, J. & Lee, J. Y. Engineering the architectural diversity of heterogeneous metallic nanocrystals. *Nat. Commun.* **4**, 1454 (2013).
18. Liu, G. *et al.* Delineating the pathways for the site-directed synthesis of individual nanoparticles on surfaces. *Proc. Natl. Acad. Sci.* **110**, 887–891 (2013).
19. Pileni, M. P. Control of the size and shape of inorganic nanocrystals at various scales from nano to macromolecules. *J. Phys. Chem. C* **111**, 9019–9038 (2007).
20. Meli, L. & Green, P. F. Aggregation and Coarsening of Ligand-Stabilized Gold Nanoparticles in Poly(methyl methacrylate) Thin Films. *ACS Nano* **2**, 1305–1312 (2008).
21. Wong, H. C. & Cabral, J. T. Mechanism and kinetics of fullerene association in polystyrene thin film mixtures. *Macromolecules* **44**, 4530 (2011).
22. Higgins, A. M. & Jones, R. A. L. Anisotropic spinodal dewetting as a route to self-assembly of patterned surfaces. *Nature* **404**, 476–478 (2000).
23. Thurn-Albrecht, T. *et al.* Ultrahigh Density Nanowire Arrays Grown in Self-Assembled Diblock Copolymer Templates. *Science* **290**, 2126–2128 (2000).
24. Sanchez-Iglesias, A. *et al.* Rapid Epitaxial Growth of Ag on Au Nanoparticles: From Au Nanorods to Core-Shell Au@Ag Octahedrons. *Chem. Eur. J.* **16**, 5558–5563 (2010).
25. Damasceno, P. F., Engel, M. & Glotzer, S. C. Predictive Self-Assembly of Polyhedra into Complex Structures. *Science* **337**, 453–456 (2012).
26. Huang, J., Kim, F., Tao, A. R., Connor, S. & Yang, P. Spontaneous formation of nanoparticle stripe patterns through dewetting. *Nat. Mater.* **4**, 896–900 (2005).
27. Michalak, W. D., Miller, J. B., Yolcu, C. & Gellman, A. J. Fabrication of metallic nanoparticles by spinodal dewetting of thin films: A high-throughput approach. *Thin Solid Films* **522**, 473–479 (2012).
28. Thompson, C. V. Solid-State Dewetting of Thin Films. *Ann. Rev. Mater. Res.* **42**, 399–434 (2012).
29. Wong, H. C. & Cabral, J. T. Spinodal clustering in polymer-nanoparticle thin films. *Phys. Rev. Lett.* **105**, 038301–038303 (2010).
30. Rycenga, M. *et al.* Controlling the Synthesis and Assembly of Silver Nanostructures for Plasmonic Applications. *Chem. Rev.* **111**, 3669–3712 (2011).
31. Cheng, W., Park, N., Walter, M. T., Hartman, M. R. & Luo, D. Nanopatterning self-assembled nanoparticle superlattices by moulding microdroplets. *Nat. Nanotechnol.* **3**, 682–690 (2008).
32. Millstone, J. E., Hurst, S. J., Metraux, G. S., Cutler, J. I. & Mirkin, C. A. Colloidal Gold and Silver Triangular Nanoprisms. *Small* **5**, 646–664 (2009).
33. Marks, L. D. & Howie, A. Multiply-twinned particles in silver catalysts. *Nature* **282**, 196–198 (1979).
34. Adelhelm, P. *et al.* Generation of Hierarchical Meso-Macro-Porous Carbon from Mesophase Pitch by Spinodal Decomposition with Polymer Templates. *Adv. Mater.* **19**, 4012–4017 (2007).
35. Dresselhaus, M. S., Jorio, A., Hofmann, M., Dresselhaus, G. & Saito, R. Perspectives on Carbon Nanotubes and Graphene Raman Spectroscopy. *Nano Lett.* **10**, 751–758 (2010).
36. Liu, H. *et al.* Single molecule detection from a large-scale SERS-active Au₇₉Ag₂₁ substrate. *Sci. Rep.* **1**, 112 (2011).
37. Erlebacher, J., Aziz, M. J., Karma, A., Dimitrov, N. & Sieradzki, K. Evolution of nanoporosity in dealloying. *Nature* **410**, 450–453 (2001).
38. Barrow, S. J., Wei, X., Baldauf, J. S., Funston, A. M. & Mulvaney, P. The surface plasmon modes of self-assembled gold nanocrystals. *Nat. Commun.* **3**, 1275 (2012).
39. Repetto, L., Batić, B. Š., Firpo, G., Piano, E. & Valbusa, U. *Appl. Phys. Lett.* **100**, 223113 (2012).
40. Zhang, L. *et al.* Effect of Residual Silver on Surface-Enhanced Raman Scattering of Dealloyed Nanoporous Gold. *J. Phys. Chem. C* **115**, 19583–19587 (2011).
41. Amarandei, G. *et al.* Effect of Au nanoparticle spatial distribution on the stability of thin polymer films. *Langmuir* **29**, 6706–6714 (2013).
42. Yamamoto, U. & Schweizer, K. S. Theory of nanoparticle diffusion in unentangled and entangled polymer melts. *J. Chem. Phys.* **135**, 224902 (2011).
43. Wong, H. C. & Cabral, J. T. Mechanism and Kinetics of Fullerene Association in Polystyrene Thin Film Mixtures. *Macromolecules* **44**, 4530–4537 (2011).



44. Peng, Z., Freunberger, S. A., Chen, Y. & Bruce, P. G. A Reversible and Higher-Rate Li-O₂ Battery. *Science* **337**, 563–566 (2012).
45. Akcora, P. *et al.* Anisotropic self-assembly of spherical polymer-grafted nanoparticles. *Nat. Mater.* **8**, 354 (2009).
46. Echtermeyer, T. J. *et al.* Strong plasmonic enhancement of photovoltage in graphene. *Nat. Commun.* **2**, 458 (2011).

Acknowledgements

Financial support from FONDECYT (Project 1085011 and 1095135) and DGICYT (Project CTQ2010-18330) are gratefully acknowledged. The authors acknowledge Dr George Amarandei for useful discussions. Part of this work was conducted under the framework of the INSPIRE programme, funded by the Irish Government's Programme for Research in Third Level Institutions, Cycle 4, National Development Plan 2007–2013. COD acknowledges support from a Science Foundation Ireland under contract no. 07/SK/B1232a, from the UCC Strategic Research Fund and from the Irish Research Council New Foundations Award.

Author contributions

C.D.V., G.A.C., M.L.V. and L.Z. contributed to precursor synthesis, design and characterization. C.O.D. conducted microscopy, spectroscopy, image and sample analysis, and wrote the manuscript. All authors contributed to analysis, writing and reviewing of the manuscript.

Additional information

Supplementary information accompanies this paper at <http://www.nature.com/scientificreports>

Competing financial interests: The authors declare no competing financial interests.

How to cite this article: Valenzuela, C.D., Carriedo, G.A., Valenzuela, M.L., Zúñiga, L. & O'Dwyer, C. Solid State Pathways to Complex Shape Evolution and Tunable Porosity during Metallic Crystal Growth. *Sci. Rep.* **3**, 2642; DOI:10.1038/srep02642 (2013).



This work is licensed under a Creative Commons Attribution-NonCommercial-ShareAlike 3.0 Unported license. To view a copy of this license, visit <http://creativecommons.org/licenses/by-nc-sa/3.0>